PCCP

ROYAL SOCIETY OF CHEMISTRY

PAPER

View Article Online
View Journal

Cite this: DOI: 10.1039/d6cp00466k

The role of sulfur vacancies on FeS_2(100) in NO dissociative adsorption: a combined *in situ* SR-XPS and DFT calculation study

Wei-Chih Hsiao, Fumihiko Ozaki, † Kozo Mukai, Shunsuke Tanaka, Daisuke Nishio-Hamane, Masahiro Fukuda, Taisuke Ozaki and Jun Yoshinobu *

Received 8th February 2026,
Accepted 16th May 2026

DOI: 10.1039/d6cp00466k

rsc.li/pccp

Sulfur vacancies (S_{vacs}) are known to change the reactivity of transition metal sulfides, but their mechanistic role in small-molecule activation remains poorly understood. Here, we carried out synchrotron radiation X-ray photoelectron spectroscopy (SR-XPS) and dispersion-corrected density functional theory (DFT-D3) calculations to elucidate how S_{vac} sites on FeS_2(100) surfaces promote nitric oxide (NO) dissociation. SR-XPS results reveal progressive Fe oxidation, Fe–N formation, and the growth of adsorbed oxygen species as a function of NO exposure. The N/O atomic ratio evolution suggests recombinative N_2 desorption from the surface. DFT-D3 calculations show that the dissociative adsorption of NO is thermodynamically more stable on the defective FeS_2(100) surface than on the defect-free surface. Based on the Brønsted–Evans–Polanyi relationship, dissociative adsorption of NO may be kinetically favorable on the defective FeS_2(100) surface. Two possible pathways are proposed: (1) O–O bond formation at S_{vac} sites and (2) oxygen-induced S–S bond cleavage to yield O–S species and new S_{mono}. The present experimental–computational study demonstrates the atomic-level role of S_{vacs} in NO activation on FeS_2(100) and provides chemical insight into defect engineering of sulfide-based catalysts for selective nitrogen oxide conversion.

1. Introduction

Nitric oxide species (NO_x), primarily emitted from fossil fuel combustion in transportation and industrial processes, contribute to severe environmental and health issues, including acid rain, photochemical smog, and respiratory illnesses. Their interaction with volatile organic compounds under sunlight can also produce ground-level ozone, further degrading air quality.[1–4] To mitigate NO_x emissions, a variety of catalytic technologies have been developed. Three-way catalysts (TWCs), employing noble metals such as Pt, Pd, and Rh, are widely used in automobiles for simultaneous reduction of NO_x and oxidation of CO and hydrocarbons.[5–7]

Among low-cost transition metal compounds, pyrite (FeS_2) has drawn increasing interest due to its abundance, nontoxic nature, and semiconducting properties. Its magnetic and optoelectronic characteristics have enabled its application in spintronics[8–10] and photovoltaics.[11] Furthermore, FeS_2 has demonstrated catalytic activity in reactions such as hydrodesulfurization (HDS),[12,13] hydrodeoxygenation (HDO),[14] and nitrogen reduction reactions (NRRs),[15] offering a sustainable alternative to noble-metal-based catalysts. The demonstrated ability of FeS_2(100) to interact with atomic nitrogen—*via* ion-beam implantation or exposure to electronically excited N_2—underscores the intrinsic surface reactivity of FeS_2 and provides a mechanistic basis for further investigations into vacancy-assisted activation of nitrogen-containing species.[16] Despite these advantages, the potential of FeS_2 in NO_x reduction remains largely underexplored. This is partly due to the high activation energy ($\sim$2.66 eV)[17] reported for NO dissociation on stoichiometric FeS_2 surfaces, which limits its effectiveness under mild conditions.

Recent studies have shown that defect engineering, particularly the introduction of sulfur vacancies (S_{vacs}), can dramatically alter the electronic properties of transition metal dichalcogenides (TMDs).[18–21] Previous studies also show that the S_{vacs} in MoS_2 can act as the active site for the hydrogen evolution reaction (HER),[22,23] while also showing potential for CO_2 capture and conversion.[24,25] The defect engineering of WS_2 is also an indispensable tool for strategically tailoring the excellent electrical and optical properties of TMDs, as well as for optimizing

The Institute for Solid State Physics, The University of Tokyo, Chiba, 277-8581, Japan. E-mail: junyoshi@issp.u-tokyo.ac.jp

† Present address: Research and Development Directorate, Japan Aerospace Exploration Agency (JAXA), Sagamihara, Kanagawa, 2525210, Japan.

electronic devices and gas sensors.[26] Multistate non-volatile memory is achieved in ReS_2 by controlling S_{vacs} induced *via* light programming,[27] and the S_{vacs} in ReS_2 also show potential in a highly selective photocatalytic CO_2 reduction.[18]

Despite the structural difference from van der Waals TMDs, FeS_2 exhibits analogous S_{vac} chemistry and catalytic behavior for comparative analysis. For FeS_2 in the catalytic field, S_{vacs} also tune the surface reactivity.[28,29] S_{vacs} of FeS_2 reduce the band gap, promote orbital hybridization, and enhance electron transfer capabilities.[30] These modifications have been linked to enhanced catalytic performance in diverse reactions, including N_2 reduction[31] and polysulfide conversion.[13] Notably, S_{vac} sites have been proposed as the active centers for the NO reduction reaction[32] and NO_2 reduction reaction[33] on FeS_2 surfaces. These findings suggest that creating sulfur-deficient FeS_2 (FeS_{2-x}) surfaces may decrease the high activation barrier for NO dissociation, providing a new route for efficient NO_x reduction.

On the other hand, mineral surfaces such as pyrite (FeS_2) and pyrrhotite ($Fe_{1-x}S$) are central to the ''iron–sulfur world'' hypothesis proposed by Wächtershäuser in the 1990s, which links Fe–S minerals to the autotrophic origin of life.[34] Beyond its catalytic applications, FeS_2 has also been implicated in origin-of-life scenarios,[35,36] with sulfur-deficient surfaces shown to adsorb L-cystine[37] and support primitive reaction networks under hydrothermal conditions.[38] Exploring NO interactions on such surfaces may not only aid environmental catalysis but also offer implications for prebiotic chemistry. Previous studies have demonstrated that the adsorption and surface transformation of nitrogen-containing molecules on FeS_2(100) are highly sensitive to surface structure and sulfur defect states. Notably, the adsorption geometry of cystine has been shown to depend on the degree of surface ordering, whereas glycine undergoes defect-mediated chemical evolution on sulfur-deficient surfaces.[39,40] These findings highlight that sulfur vacancy sites serve as key reactive centres not only for simple adsorbates but also for more complex, nitrogen-containing molecules. Recent near-ambient-pressure X-ray photoelectron spectroscopy (NAP-XPS) studies revealed that FeS_2 can adsorb L-cystine even under O_2 and CO_2 atmospheres, bridging surface processes relevant to both modern environmental catalysis and early Earth prebiotic chemistry.[41] Moreover, UV-irradiated FeS_2 has been shown to photocatalytically fix atmospheric nitrogen into ammonium salts under both Earth- and Mars-like conditions, highlighting its dual role as a catalytic and prebiotic surface.[42] These findings indicate that FeS_2 is active not only toward nitrogen oxides but also toward ammonium-related reactions, underscoring the broader relevance of nitrogen-containing species on FeS_2 surfaces and motivating further surface science investigation.

In this study, we investigated the role of S_{vacs} in facilitating NO dissociation on an FeS_2(100) surface. Using *in situ* synchrotron radiation X-ray photoelectron spectroscopy (SR-XPS), we examined the surface processes of NO on both low-/high-S_{vac} surfaces. Density functional theory (DFT) calculations, including D3 van der Waals corrections (DFT-D3), were employed to simulate the adsorption energetics, dissociation pathways, and binding energies of residual oxygen species. The present findings deliver atomic-scale insights into NO activation mechanisms on FeS_2(100) and underscore the effectiveness of defect engineering in transition metal sulfides as a strategy for enhancing NO_x reduction catalysis.

2. Experimental

2.1. Sample preparation

A natural FeS_2 crystal from Spain (1.0 cm^3) was used as the sample. FeS_2(100) surfaces were prepared by cutting 1 cm^2 × 0.1 cm slices along the ⟨100⟩ direction from a cubic natural crystal, similar to the preparation of the low-S_{vac} FeS_2(100) surface in the previous study.[43] Each slice was then divided into two 0.5 cm^2 samples and mirror-polished. Prior to installing them in an ultra-high-vacuum (UHV) chamber, both samples were cleaned by sequential ultrasonic treatment in (1) acetone and (2) ethanol, for 30 minutes each. To minimize surface carbon contamination, the low-S_{vac} sample was lightly etched in a dilute acid solution (3 drops of 14 M HCl in 40 mL H_2O) for 2 minutes, followed by a procedure reported in the previous research.[43] The S_{vac} concentrations on FeS_2(100) surfaces were controlled by Ar^+ sputtering at 200 eV and 600 eV for the low- and high-S_{vac} samples at 2.0 μA for 10 minutes, respectively, followed by annealing at 560 K for 5 minutes. We observed a (1 × 1) LEED pattern of a low-S_{vac} sample, as shown in Fig. S1.

2.2. Synchrotron radiation X-ray photoelectron spectroscopy

SR-XPS measurements were performed in a chamber equipped with a hemispherical electron energy analyzer (Scienta SES200) at BL-13B of Photon Factory, KEK, Japan.[44] The base pressure in the UHV chamber was below 2×10^{-10} mbar. The incident and emission angles were 65° and 0°, respectively. Samples were exposed to $NO_{(g)}$ in a preparation vacuum chamber. All XPS spectra were acquired at room temperature using a photon energy of 800 eV. Binding energies were calibrated against the Fermi level of deposited gold on the sample holder. The total energy resolution of the XPS system was approximately 0.26 eV. The binding energies and line widths of the Fe 2p, S 2p, N 1s, and O1s core levels were determined by fitting the spectra with a Voigt function and a Shirley-type background.

2.3. DFT calculations

DFT calculations were performed using the OpenMX code.[45,46] For the exchange–correlation functional, a generalized gradient approximation by the Perdew, Burke, and Ernzerhof functional (GGA-PBE) was used.[47] For each Fe atom, three, two, and one optimized radial functions were allocated for the s, p, and d orbitals, respectively. A cutoff radius of 5.5 Bohr was chosen for the basis functions as denoted by Fe5.5H-s3p2d1. For the S atom, S7.0-s2p2d1f1 basis functions were adopted. For the N atom, N6.0-s2p2d1 basis functions were adopted. For the O atom, O6.0-s2p2d1 basis functions were adopted. The basis functions and pseudopotential used were validated by the delta gauge method.[48] A (1 × 3 × 3) mesh of *k* points and a regular

mesh size of 350 Ry in real space were used for the numerical integrations and for the solution of the Poisson equation.

The geometry was optimized using a threshold of 0.0003 Hartree per Bohr for the forces. The FeS_2 surface was modeled by a $(3 \times 2 \times 2)$ slab with six Fe layers along the *a*-axis, where the unit cell of FeS_2 contains two Fe layers in this direction. A vacuum region of 20 Å was introduced along the *a*-axis. The slab contained 48 Fe and 96 S atoms, enabling the description of surface, subsurface, and bulk-like layers, with slab models shown in Fig. S5. No atoms were fixed during the calculations. The vdW interaction was taken into account in the dispersion-corrected density functional theory approach.[49,50] In the geometry optimization calculations, conventional pseudopotentials and optimized basis functions provided on the OpenMX website were used.[48,51–54] Spin-polarized calculations were performed in this study. For the adsorption systems, unequal initial spin populations were assigned to the adsorbed N, O, and the Fe atoms neighboring the S_{vac} site as the initial state. After self-consistent-field (SCF) convergence, the results showed almost no residual spin polarization.

The core-level binding energies of the O 1s states were calculated by the delta self-consistent field (ΔSCF) method,[55] in which the final states with a core hole were self-consistently determined by the penalty function method[55] and the exact Coulomb cutoff method[56] with fully relativistic norm-conserving pseudopotentials.[52,53] This approach has been applied to several substrates (Pd/Cu, MoS_2, Si on ZrB_2, Ge on ZrB_2, borophene on Ag, and polycarbonate on Ti/Al/TiAl).[57–62] The structures used for the ΔSCF calculations were taken from the fully optimized geometries obtained in the geometry optimization step, and no further structural relaxation was performed during the core-level calculations. For the geometry optimization, the O pseudopotential treated six valence electrons ($2s^2 2p^4$), whereas for the O 1s ΔSCF calculations, a different norm-conserving pseudopotential was employed in which the 1s state was also treated explicitly, resulting in eight explicitly treated electrons ($1s^2 2s^2 2p^4$). Fully relativistic pseudopotentials and pseudoatomic orbitals for O 1s excitation were used for core-level excitation calculations.[54,55] The systems were treated as insulators, and the exact Coulomb cutoff method was used to eliminate spurious Coulombic interactions between core-hole images under periodic boundary conditions. A $(2 \times 3 \times 3)$ slab model was adopted for the core-level calculations. Compared with the slab used for geometry optimization, the model was expanded in the *b*- and *c*-axis directions and reduced along the *a*-axis as a compromise between computational cost and accuracy. Noncollinear spin polarization and spin–orbit coupling were included in absolute binding energy calculations. The molecular and surface structure models presented in this work were rendered using VESTA software.[63,64]

3. Results and discussion

3.1. SR-XPS investigation of NO adsorption on $FeS_2(100)$

3.1.1. Comparative NO adsorption on low- and high-S_{vac} surfaces. To investigate the role of S_{vacs} on an $FeS_2(100)$ surface in modulating reactivity toward NO, we compared low- and high-S_{vac} surfaces under the same NO exposure conditions. This experiment aimed to establish a direct correlation between the vacancy density and NO adsorption behavior.

Fig. 1 presents the models of ideal and defective $FeS_2(100)$ surfaces. Key surface atomic sites are labeled, including bulk Fe (Fe_{bulk}, 6-coordinated), surface Fe (Fe_{surf}, 5-coordinated), unsaturated Fe (Fe_{unsat}, 4-coordinated), surface S (S_{surf}), sulfur monomer (S_{mono}), and bulk S (S_{bulk}).

The S_{vac} concentration was tuned *via* controlled Ar^+ sputtering and quantified from the S_{mono} component in the S 2p spectra on the clean surface (Fig. 2(b) and Table 1). On the low-S_{vac} surface, S_{mono} accounted for 10.6% of the total S signal, increasing to 23.9% for the high-S_{vac} surface, confirming a substantial enhancement in vacancy density. This controlled variation provides a platform for probing defect–reactivity relationships.

During NO exposure, the low- and high-S_{vac} surfaces were simultaneously dosed in the same preparation vacuum chamber at room temperature. Post-exposure SR-XPS spectra (Fe 2p, S 2p, N 1s, and O 1s; Fig. 2 and Table 1) exhibit pronounced oxidation features in the Fe 2p and O 1s regions. The N 1s signal is weak, with an N/O atomic ratio of ~0.01 (corrected for the photo-ionization cross-section at $h\nu$ = 800 eV and the inelastic mean free path of electron kinetic energy), indicating that most of the nitrogen recombines and desorbs as N_2 from the surface, which will be discussed later. A residual N 1s feature is found at 399.4–399.5 eV, which is characteristic of Fe–N coordination.[65]

The O 1s region resolves into two distinct peaks, P1 at 529.7–529.8 eV and P2 at 531.1–531.2 eV, revealing the coexistence of

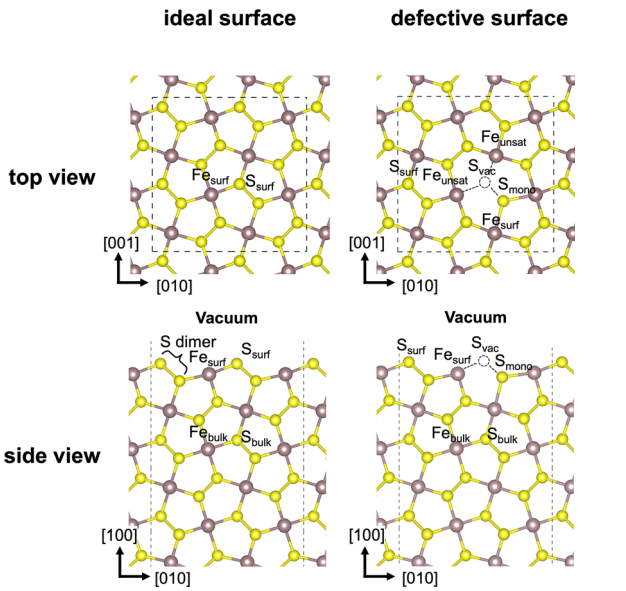

Fig. 1 Structure of defect-free and defective $FeS_2(100)$ surface models. Top and side views are shown for both models. The light-yellow spheres represent sulfur atoms, and the brown spheres represent iron atoms. In the defective model, key atomic sites are labeled, including surface Fe (Fe_{surf}), unsaturated Fe (Fe_{unsat}), surface S (S_{surf}), sulfur monomer (S_{mono}), sulfur vacancies (S_{vacs}), and bulk Fe and S atoms (Fe_{bulk} and S_{bulk}).

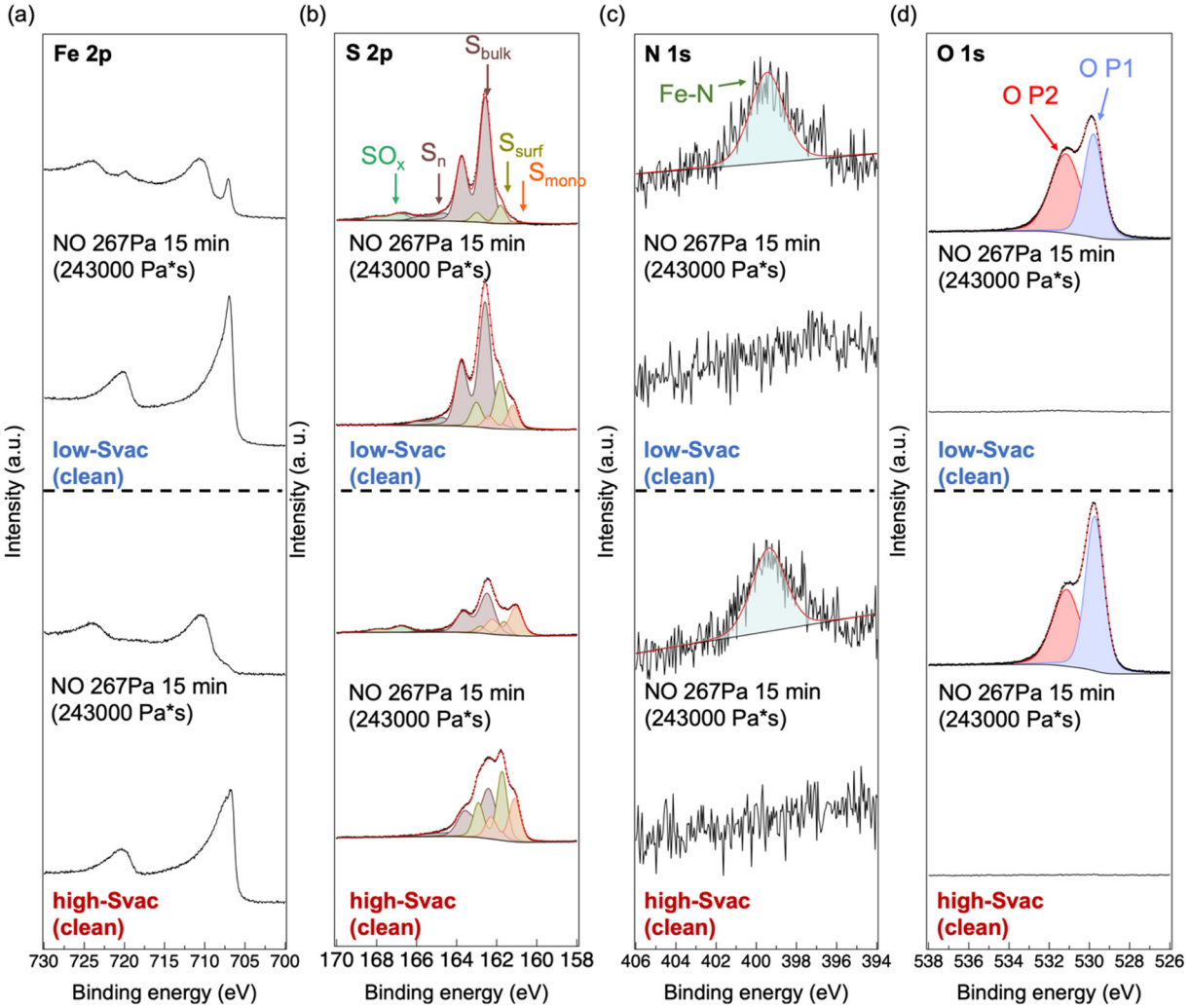

Fig. 2 SR-XPS spectra of FeS_2(100) surfaces with low- and high-S_{vacs} before and after exposure to 2.67 Pa NO for 15 min at room temperature. (upper panel) Low-S_{vac} surface; (lower panel) high-S_{vac} surface. (a) Fe 2p, (b) S 2p, (c) N 1s, and (d) O 1s regions are shown from left to right, respectively. Deconvoluted components are overlaid in the S 2p, N 1s, and O 1s spectra. Peak fitting was conducted using Voigt peaks with a Shirley background. Sulfur components are deconvoluted into S_{vacs}, S_{surf}, S_{bulk}, S_n, and SO_x species. Oxygen species are labeled as O P1 and O P2, and nitrogen species are assigned as Fe–N bonding.

Table 1 Peak analysis of SR-XPS spectra for low-S_{vac} and high-S_{vac} FeS_2(100) surfaces before and after NO exposure (267 Pa, 15 min). Binding energies (BEs), full width at half maximum (FWHM) values, and relative component ratios are shown for the S 2p, O 1s, and N 1s regions. Sulfur components are deconvoluted into S_{mono}, S_{surf}, S_{bulk}, S_n, and SO_x species. Oxygen species are labeled as O P1 and O P2, and nitrogen species are assigned as Fe–N bonding

FeS_2(100) Sample	Exp. condition		S 2p					O 1s		N 1s
			S_{mono}	S_{surf}	S_{bulk}	S_n	SO_x	O P1	O P2	Fe–N
Low-S_{vacs}	Clean	B.E. (eV)	161.2	161.8	162.6	164.7				
		FWHM (eV)	0.6	0.6	0.7	1.0				
		Ratio (%)	10.6	21.7	62.2	5.5				
	NO 267 Pa 15 min	B.E. (eV)	161.2	161.8	162.6	164.7	166.8	529.8	531.2	399.5
		FWHM (eV)	0.4	0.6	0.7	1.0	1.1	1.1	1.8	2.0
		Ratio (%)	0.9	9.5	76.6	6.6	6.4	45.3	54.7	
High-S_{vacs}	Clean	B.E. (eV)	161.1	161.7	162.4	164.3				
		FWHM (eV)	0.7	0.6	0.9	1.6				
		Ratio (%)	23.9	34.8	36.6	4.6				
	NO 267 Pa 15 min	B.E. (eV)	161.0	161.6	162.5	164.7	166.8	529.7	531.1	399.4
		FWHM (eV)	0.8	0.6	0.9	0.9	1.0	1.1	1.6	2.0
		Ratio (%)	30.2	11.0	48.3	2.6	7.9	57.2	42.8	

different oxygen species after NO dissociation. O 1s peaks at binding energies of around 529.7–530.5 eV are reported as atomic O on the FeS_2 surface,[41,66,67] while O 1s peaks at binding energies of around 531.0–531.3 eV are assigned as adsorbed O_2 or FeOOH/$FeSO_4$ according to the previous studies.[41,67] Higher binding energy species around 532.0 eV are assigned as OH or O_2 species from the dissociative adsorbed H_2O.[66] Note that, in the case of $NO_{(g)}$, an O 1s peak was observed at 538.8 eV and multiplet splitting peaks of N 1s were observed at 405.8 eV and 407.1 eV;[68] in the case of $NO_{(ads)}$, an O 1s peak was observed at 531.8 eV and multiplet splitting peaks of N 1s were observed at 396.8 eV.[69] Combined with Fe oxidation and N 1s detection, these results clearly indicate dissociative adsorption of NO on FeS_2(100) with S_{vacs}. The process can be summarized as follows:

$$NO_{(g)} \rightarrow N_{(ads)} + O_{(ads)} \quad \Delta H_{\text{ideal } FeS_2} = -0.17 \text{ eV} \tag{1.1}$$

$$\Delta H_{\text{defective } FeS_2} = -2.60 \text{ eV} \tag{1.2}$$

$$NO_{(g)} + N_{(ads)} + O_{(ads)} \rightarrow N_{2(g)} + 2O_{(ads)} \quad \Delta H_{\text{defective } FeS_2} = -1.61 \text{ eV} \tag{2}$$

Overall conversion:

$$2NO_{(g)} \rightarrow N_{2(g)} + 2O_{(ads)} \quad \Delta H_{\text{defective } FeS_2} = -4.21 \text{ eV} \tag{3}$$

(ΔH values are evaluated from DFT-D3 calculations, which will be discussed in Section 3.2.2.)

Fe 2p spectra (Fig. 2(a)) show that the low-S_{vac} surface retains a clear Fe^{2+} component (~707.4 eV), indicating limited oxidation, while the high-S_{vac} surface exhibits a marked shift to Fe^{3+} (~710.9 eV), consistent with extensive oxidation.[70] This difference supports the view that S_{vac} sites act as active sites for NO dissociation, selectively promoting Fe oxidation.

The assignments of S 2p spectra follow established literature values: S_{mono} (160.95–161.25 eV), S_{surf} (161.70–162.00 eV), S_{bulk} (162.35–162.70 eV), polysulfide S_n^0/S_n^{2-} or core–hole effects (163.40–164.50 eV), and SO_x species (166.20–168.50 eV).[43,71–76] After NO exposure, the S_{mono} and S_{surf} intensities decrease (Fig. 2(b)) on both surfaces. The decreased intensity of S_{mono} suggests O incorporation at S_{vac} sites, while the concurrent reduction of S_{surf} indicates that adjacent surface sulfur dimers also participate in the NO dissociation process (see (Fig. 2)).

3.1.2. Evolution of surface chemistry during progressive NO adsorption on high-S_{vac} surfaces. To probe the stepwise reaction of NO dissociation at defective sites, a progressive NO exposure experiment was performed on a high-S_{vac} FeS_2(100) surface at 2 Pa as a function of time (from 0 to 150 min), and finally exposure up to 243 000 Pa s.

The SR-XPS spectra (Fig. 3) capture the sequential evolution of surface chemistry during NO exposure, with the N/O atomic ratio profile (Fig. 4) providing further insight into the reaction sequence. Very initially, NO adsorption at S_{vac} sites yields a relatively high N/O atomic ratio (~0.66). As exposure progresses, the ratio steadily decreases to ~0.08, indicating that adsorbed nitrogen reacts with NO to form $N_{2(g)}$, which then desorbs, leaving oxygen on the surface (discussed later in the DFT-D3 calculation section).

The N 1s spectra at a binding energy of about 399.4 eV show the emergence of Fe–N bonding,[65] while the O 1s spectra reveal the growth of two different oxygen components, confirming the formation of different oxygen-containing species. The reproducibility of these spectral changes across a series of spectra indicates a stepwise dissociative adsorption process at S_{vac} sites. Changes in the oxygen environment are further detailed in Fig. 5. Upon early exposure, the O 1s spectra display both P1 (low-binding-energy) and P2 (high-binding-energy) species, with P2 intensifying markedly at higher O coverage. This trend

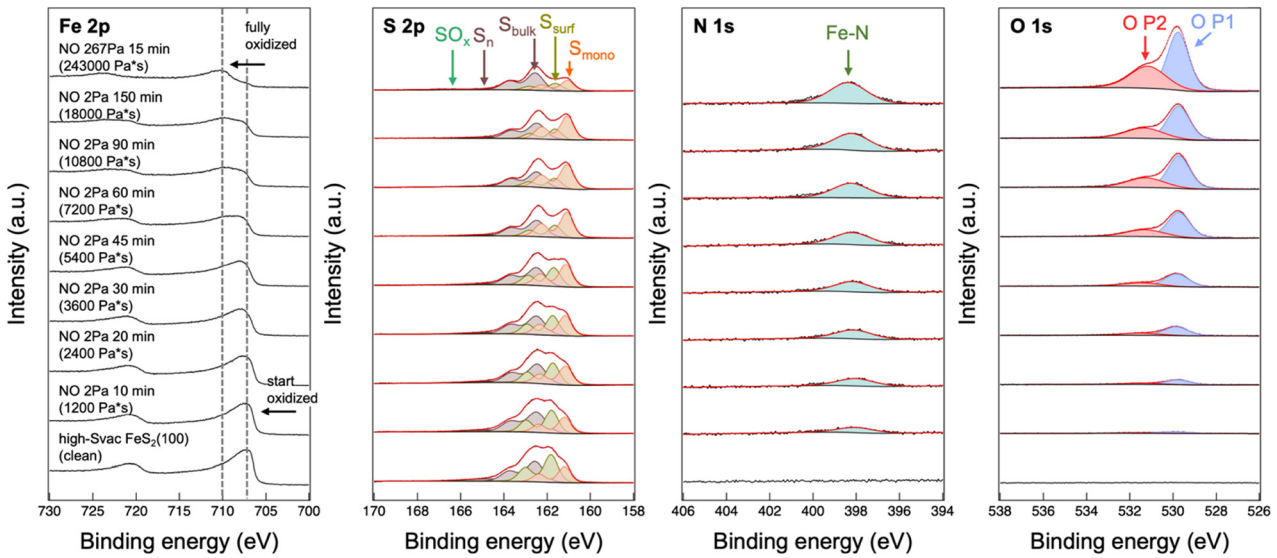

Fig. 3 Progressive SR-XPS spectra of high-S_{vac} FeS_2(100) during NO exposure. Spectra were acquired after sequential exposure to 2 Pa NO for increasing durations (10–150 min), followed by a final 15 min exposure at 267 Pa. Fe 2p, S 2p, N 1s, and O 1s regions. Deconvoluted peaks in S 2p correspond to S_{mono}, S_{surf}, S_{bulk}, S_n, and SO_x components; O 1s peaks are assigned to O P1 and O P2.

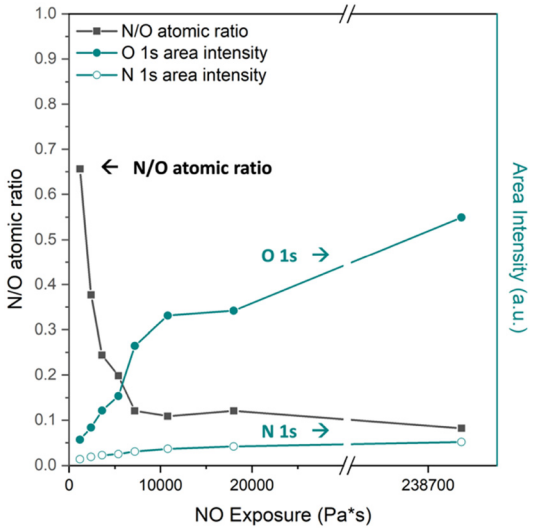

Fig. 4 SR-XPS evolution of the N 1s and O 1s core-level signals during progressive NO exposure on high-S_{vac} FeS_2(100). Spectra were acquired at 2 Pa NO for increasing exposure times (10–150 min), followed by a final 15 min exposure at 267 Pa. The N/O atomic ratio (left axis) and integrated peak areas of N 1s and O 1s (right axis) are plotted as a function of NO exposure dose (Pa s).

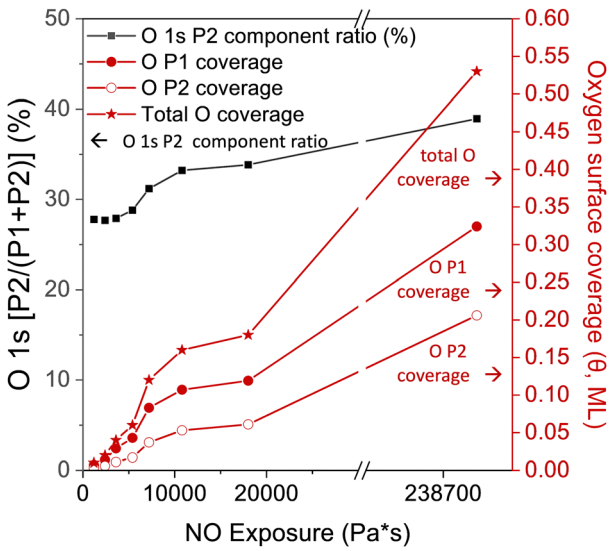

Fig. 5 SR-XPS evolution of O 1s spectral components and surface oxygen coverage during progressive NO exposure on high-S_{vac} FeS_2(100). (left axis) O P1 and P2 peak intensities and their relative P2 component ratio [P2/(P1 + P2)] as a function of NO exposure dose (Pa s). (right axis) Estimated oxygen surface coverage (θ, in monolayer, ML). Spectra were acquired at 2 Pa NO for increasing exposure times (10–150 min), followed by a final 15 min exposure at 267 Pa.

suggests that P2 formation is favored at elevated oxygen surface densities, likely *via* the interaction between adsorbed O atoms to form an O–O bond (discussed later in the DFT-D3 calculation section).

The sulfur component trends are summarized in Fig. 6. The S_{surf} component decreases continuously with increasing exposure, while S_{mono} exhibits an initial increase followed by a

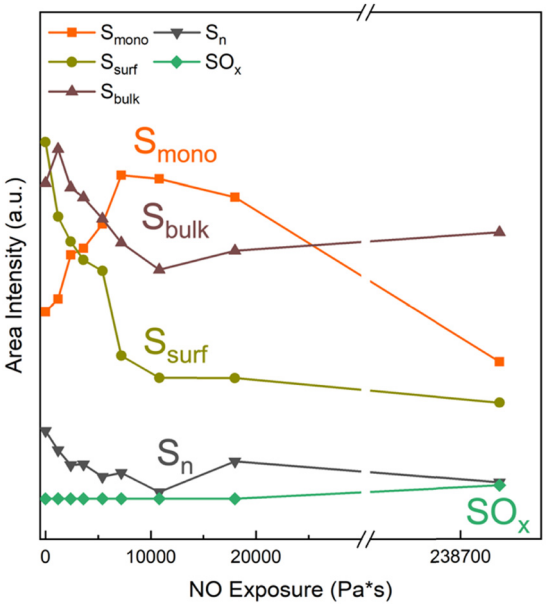

Fig. 6 SR-XPS evolution of S 2p spectral components during progressive NO exposure on high-S_{vac} FeS_2(100). Area intensities of deconvoluted sulfur species (S_{mono}, S_{surf}, S_{bulk}, S_n, and SO_x) are plotted as a function of NO exposure dose (Pa s). Spectra were acquired at 2 Pa NO for increasing exposure times (10–150 min), followed by a final 15 min exposure at 267 Pa.

decline. This behavior suggests that, in the early stages of reaction, the interaction between an adsorbed oxygen atom and surface sulfur dimer disrupts the S–S bond, and one of the surface sulfur atoms becomes S_{mono} (discussed later in the DFT-D3 calculation section). At later stages, as O coverage increases, S_{vac} sites become occupied by oxygen atoms, leading to a net decrease in S_{mono}.

3.2. DFT calculations on NO dissociation mechanisms

The bulk FeS_2 structural parameters obtained from DFT-D3 calculations are as follows: S–S bond length (d_{S-S}) = 2.22 Å, Fe–S bond length (d_{Fe-S}) = 2.26 Å, and lattice constant (a_0) = 5.417 Å. These values are consistent with the reported experimental data (d_{S-S} = 2.15 Å, d_{Fe-S} = 2.26 Å, and a_0 = 5.417 Å).[19] Based on the geometry optimizations shown in Fig. S2, S3 and Tables S1, S2, the most stable NO adsorption site on the defect-free FeS_2(100) surface involves N-end coordination to a surface Fe atop site, in agreement with previous studies.[17] For the defective FeS_2(100) surface, the most stable configuration likewise features N-end coordination to the S_{vac} site, consistent with the previous report.[32]

3.2.1. O 1s core-level binding energy calculations for identifying residual oxygen species. The presence of two distinct oxygen species in the SR-XPS O 1s spectra after $NO_{(g)}$ exposure at room temperature motivated an investigation into their geometries and chemical environments on an FeS_2(100) surface. To this end, oxygen-adsorbed models were first constructed for the defect-free FeS_2(100) surface to assess whether the residual O species could interact with surface atoms adjacent to S_{vac} sites.

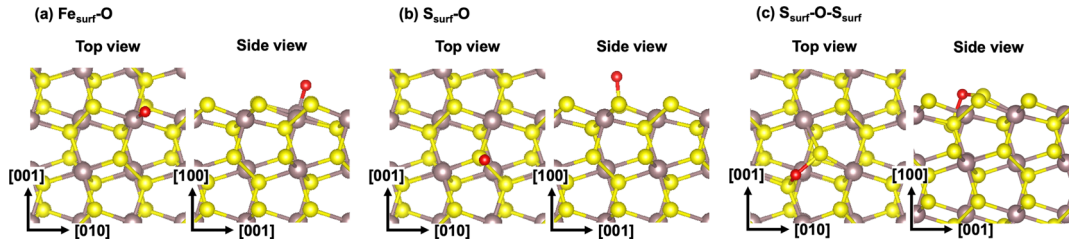

Fig. 7 Top- and side-view structural models used for absolute O 1s binding energy calculations on the defect-free FeS_2(100) surface. (a) Fe_{surf}–O: single oxygen atom bonded atop the iron site. (b) S_{surf}–O: single oxygen atom bonded atop the sulfur site. (c) S_{surf}–O–S_{surf}: oxygen atom simultaneously bonded between a surface sulfur and a subsurface sulfur, forming a bridge. The yellow, brown, and red spheres represent sulfur, iron, and oxygen atoms, respectively.

The optimized geometries and calculated O 1s binding energies for the defect-free surface are shown in Fig. 7 and Table 2. Among the adsorption configurations examined, only oxygen bound to the atop site of S_{surf} yields a binding energy (529.46 eV) close to the experimental P1 feature (529.7–529.8 eV).

Defective surface models used for O 1s absolute binding energy calculations are presented in Fig. 8 and Table 3. Oxygen adsorbed directly at the S_{vac} site (Fig. 8(b), (c) and Table 3(b), (c) (O_{Svac})) gives the computed binding energies of 529.26–529.75 eV, in good agreement with the P1 species. Another plausible configuration involves oxygen adsorbed on a surface sulfur atop site with a binding energy of 529.69 eV (Fig. 8(c) and Table 3(c) ($O_{S\text{-}atop}$)), also matching the P1 range. In addition, the O on the bridge side between Fe_{unsat} and S_{surf} geometries (Fig. 8(d) and Table 3(d) ($O_{bridge\text{-}1}$ and $O_{bridge\text{-}2}$)), where dissociated O interacts with one side of a sulfur dimer to disrupt the S–S bond and the other side interacts to form a new S_{mono} species, yielding a binding energy of 529.22–529.67 eV. These results further support an additional contribution to P1 and the observed S_{mono} increases at the initial stage of NO exposure.

Table 2 Comparison of computed and experimental O 1s binding energies for defect-free FeS_2(100) adsorption models

Defect-free FeS_2(100) surface model				
Model	O Species	State	Experiment B.E. (eV)	Computed B.E. (eV)
(a)	Fe_{surf}–O	O 1s	529.7–529.8 (P1)	527.31
(b)	S_{surf}–O	O 1s	531.1–531.2 (P2)	529.46
(c)	S_{surf}–O–S_{surf}	O 1s		530.57

To account for the observed P2 species (531.1–531.2 eV), several geometries were evaluated. As shown in Fig. 8(b), oxygen bound to a surface Fe atop site yields a significantly lower binding energy of 527.40 eV (Table 3(b) ($O_{Fe\text{-}atop}$)). By comparison, oxygen occupying S-atop sites is relatively more stable than the Fe-atop sites both on the defect-free (−0.64 eV) and defective (−0.43 eV) FeS_2(100) surfaces, as shown in Fig. S4. Therefore, the $O_{Fe\text{-}atop}$ configuration can therefore be excluded

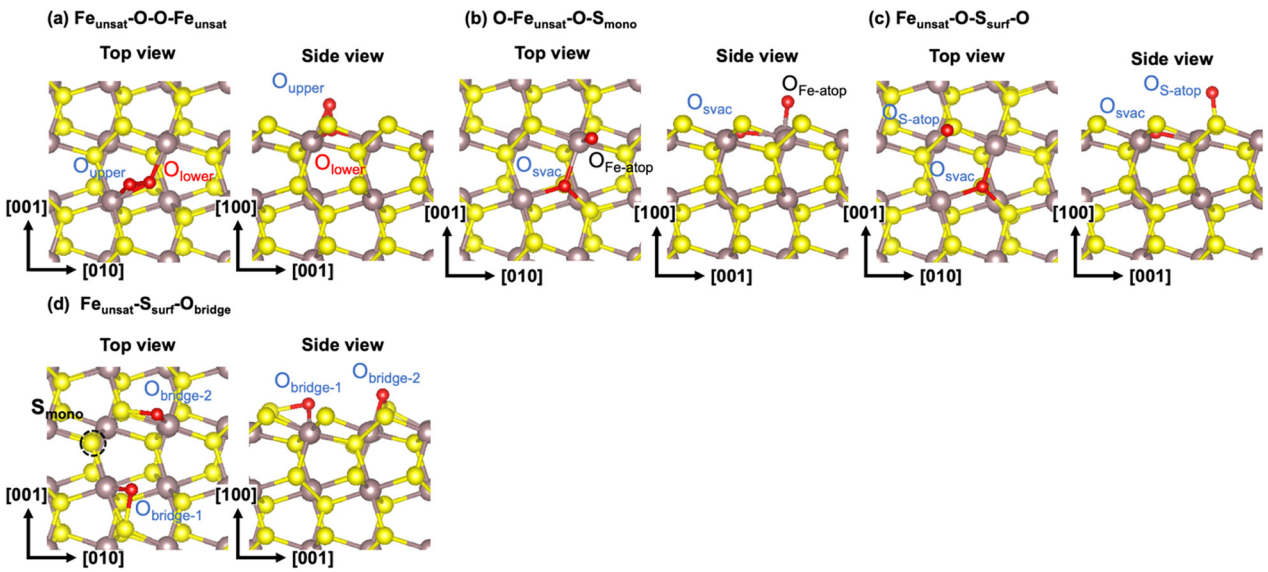

Fig. 8 Top- and side-view structural models used for absolute O 1s binding energy calculations on defective FeS_2(100) surfaces. (a) Fe_{unsat}–O–O–Fe_{unsat}: oxygen atoms bridging two adjacent surface unsaturated Fe atoms neighboring S_{vacs}. (b) O–Fe_{unsat}–O–S_{mono}: one oxygen atom bound at the S_{vac} site, and the atop site of unsaturated Fe coordinated with an additional surface O. (c) Fe_{unsat}–O–S_{surf}–O: one oxygen atom bound at the S_{vac} site, and the atop site of S_{surf} coordinated with an additional surface O. (d) Fe_{unsat}–S_{surf}–O: oxygen atoms bridging the unsaturated Fe atoms neighboring S_{surf}. The yellow, brown, and red spheres represent sulfur, iron, and oxygen atoms, respectively.

Table 3 Comparison of computed and experimental O 1s binding energies for adsorption models on defective $FeS_2(100)$ surfaces

Defective $FeS_2(100)$ surface model				
Model	O Species	State	Experiment B.E. (eV)	Computed B.E. (eV)
(a)	Fe_{unsat}–O–O–Fe_{unsat}	O 1s	529.7–529.8 (P1)	O_{upper} 529.81 O_{lower} 531.13
(b)	O–Fe_{unsat}–O–S_{mono}	O 1s		$O_{Fe\text{-}atop}$ 527.40 O_{Svacs} 529.26
(c)	Fe_{unsat}–O–S_{surf}–O	O 1s	531.1–531.2 (P2)	$O_{S\text{-}atop}$ 529.69 O_{Svacs} 529.75
(d)	Fe_{unsat}–S_{surf}–O_{bridge}	O 1s		$O_{bridge\text{-}1}$ 529.22 $O_{bridge\text{-}2}$ 529.67

as a candidate for the P2 species. In contrast, the O–O configuration at the S_{vac} site shown in Fig. 8(a) and Table 3(a) produces a calculated binding energy of 531.13 eV for O_{lower}, which is consistent with P2; on the other hand, O_{upper} shows 529.81 eV, matching P1.

In summary, oxygen species adsorbed at the S_{vac} site, the S atop site, the bridge side between Fe_{unsat} and S_{surf}, and O_{upper} in the O–O species contribute to P1, while O_{lower} in the O–O species is the probable source of P2. These assignments are supported by the progressive NO exposure experiments on high-S_{vac} $FeS_2(100)$ (Fig. 5), where the P2 component ratio increases from 0.26 at the early stage to ~0.4 at higher exposure. This trend suggests that P2 (O_{lower}) is linked to O–O species at S_{vac} sites, while P1 originates from multiple adsorption geometries, including a fraction (~0.4 of P1 at the final stage) derived from O_{upper} in the O–O species and the remainder from other oxygen configurations.

3.2.2. Reaction pathways for NO dissociation and N_2 formation on defective surfaces. The calculated dissociative adsorption pathways of NO on both defect-free and defective $FeS_2(100)$ surfaces are shown in Fig. 9(a)–(c). On the defect-free surface (black), NO adsorbs most stably with the nitrogen atom coordinated to a surface Fe site, with an adsorption energy of −2.01 eV. However, dissociation into N_{ads} and O_{ads} is thermodynamically unfavorable, with the final state lying +1.84 eV above the molecular adsorption state. In contrast, Fig. 9(a′)–(c′) illustrates the corresponding pathway on a defective surface containing the S_{vac} site. In this case, NO adsorption is more exothermic (−3.10 eV) and the dissociation state becomes mildly endothermic (+0.50 eV), representing a substantial reduction in energy relative to the defect-free surface. The DFT-D3 results show that the dissociated adsorption configuration of NO is energetically much more stabilized on the defective $FeS_2(100)$ surface than on the defect-free surface. In contrast to the defect-free surface, these results indicate that sulfur-vacancy sites preferentially stabilize the dissociated N and O species. Although transition-state calculations were not carried out in this study, the substantial stabilization of the dissociated state qualitatively suggests that NO dissociation may proceed more preferably on the defective surface, in line with a Brønsted–Evans–Polanyi relationship. According to the geometry optimization, the pronounced energy difference between the dissociated final states on the defect-free $FeS_2(100)$ surface (Fig. 9(c)) and the defective surface (Fig. 9(c′)) can be attributed to the much stronger stabilization of the dissociation fragments—especially N_{ads}—in the presence of the S_{vac}. On the defect-free surface, N and O adsorb on relatively saturated sites with limited coordination, resulting in a high-energy final state. By contrast, one S_{vac} creates two under-coordinated local Fe_{unsat} sites, enabling N_{ads} to form stronger Fe–N interactions, thereby stabilizing the dissociated state and lowering the dissociation energy.

In order to investigate the experimentally observed low N/O atomic ratio after prolonged NO exposure (Fig. 9(d′), (e′), (f′) and (g′)), further calculations were carried out to model the reaction between a pre-adsorbed nitrogen atom and an incoming NO molecule. Fig. 9(d′) shows the structure of an additional NO adsorption on the defective FeS_2 surface after the initial dissociative adsorption of NO. According to the calculated results, the second NO molecule that adsorbs onto the N top, forming an N–N bond, makes the energy more stable, decreasing from −2.60 eV to −4.04 eV. After $N_{2(g)}$ desorbs as shown in Fig. 9(e′), the total energy becomes more thermodynamically stable, decreasing from −4.04 eV to −4.21 eV. Next, the oxygen atom interacts with a neighboring surface sulfur dimer, breaking the S–S bond and generating a new S_{mono} species (Fig. 9(f′)), which results in further stabilization from −4.21 eV to −4.28 eV. This is the most likely path for S_{mono} formation from the interaction between the adsorbed O species and the sulfur dimer during the reaction.

Finally, two plausible mechanistic pathways for N_2 formation and residual O stabilization were identified. In path 1 (Fig. 9(g′-1)), both oxygen atoms migrate toward the S_{vac} site, forming a new O–O bond. The computed O 1s binding energies show that the lower O atom (O_{lower}, 531.13 eV) corresponds to the experimental P2 species, while the upper O atom (O_{upper}, 529.81 eV) matches P1 and is thermodynamically stable from −4.28 eV to −4.67 eV. In the case of Path 2 (Fig. 9(g′-2)), the other oxygen atom occupies the S_{vac} site (Fig. 9(g′-2)). This pathway explains the observed initial S_{mono} increase and decrease at prolonged NO exposure in Fig. 6 during progressive NO exposure, and the final geometry is thermodynamically stable. Both oxygen atoms in this configuration yield binding energies consistent with the P1 feature and are thermodynamically stable from −4.28 eV to −6.12 eV.

These two pathways account for the experimentally observed oxygen species in XPS (P1 and P2) and the intensity changes of sulfur species at high NO doses. Path 1 associates P2 formation with O–O bond formation at the S_{vac} site, whereas Path 2 links the transient increase in S_{mono} to oxygen–sulfur interactions before S_{vac} occupation.

On the whole, in the first experiment, we compared NO adsorption on $FeS_2(100)$ surfaces with low- and high-sulfur-vacancy (S_{vac}) concentrations. The results showed that Fe on the

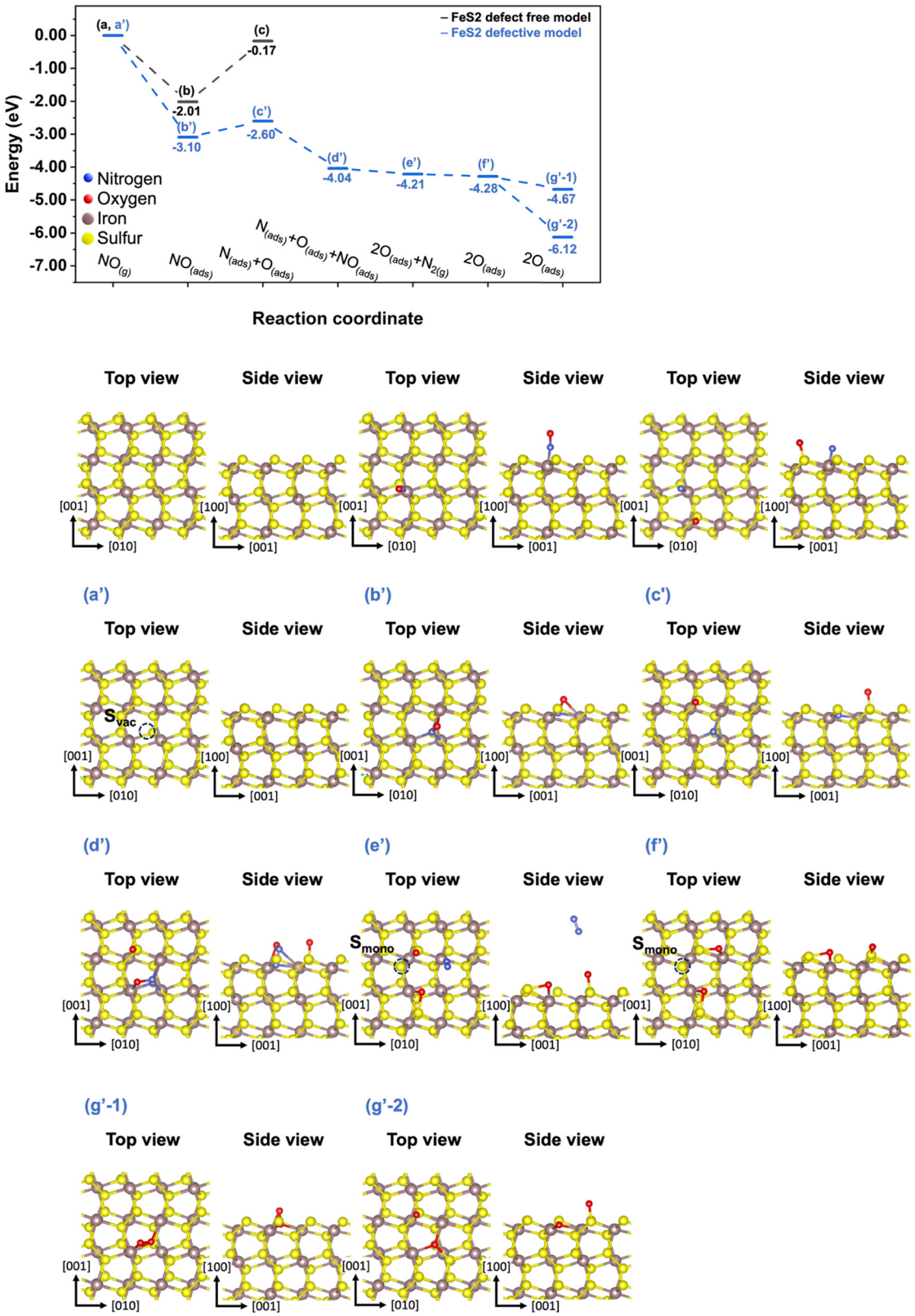

Fig. 9 DFT-D3 computed energy profiles for the dissociative adsorption of NO on FeS_2(100) surfaces, comparing the defect-free model (black line) and the S-vacancy model (blue line). Gas-phase molecules not explicitly shown in the structures were treated using isolated gas-phase calculations.

low-S_{vac} surface was only partially oxidized, whereas the high-S_{vac} surface exhibited full oxidation. These findings indicate that S_{vac} sites serve as active sites for NO dissociative adsorption. In addition, the low N/O atomic ratio ($\sim$0.01) suggests

that most nitrogen species desorbed as N_2 from the surface after reaction. To investigate this process in detail, we carried out a second experiment as a function of NO exposure time on the high-S_{vac} surface. The results confirmed the reproducibility of the reaction processes and revealed the oxidation sequence through Fe 2p spectral changes, along with semi-quantitative analysis of surface composition using S 2p, N 1s, and O 1s spectra. These results showed that the N/O atomic ratio is initially close to 1.0 ($\sim$0.66), indicating that both nitrogen and oxygen species were present on the surface at the early stages of the reaction and that the N species desorbed upon further $NO_{(g)}$ exposure, which anticipated the conversion into $N_{2(g)}$. Furthermore, changes in the S 2p region suggest that the surface sulfur dimer participates in the reaction. Complementing these experimental observations, DFT-D3 calculations provided atomistic insight into the surface reactions. Using the ΔSCF method, the absolute O 1s binding energies of possible surface-bound oxygen species were computed to assist in peak assignment. We have proposed a reaction mechanism that is consistent with both the experimental trends and calculated binding energies. The present mechanism is also thermodynamically favorable, further supporting the interpretation of the observed O 1s features.

4. Conclusions

The present study elucidates the atomic-level mechanism by which S_{vac} promote nitric oxide (NO) dissociative adsorption on $FeS_2(100)$ surfaces using a combined SR-XPS and DFT-D3 approach.

SR-XPS experiments reveal that high-S_{vac} surfaces undergo pronounced Fe oxidation, concurrent with reductions in S_{surf} and S_{mono}, the appearance of Fe–N bonding, and the formation of two distinct oxygen species. The N/O atomic ratio as a function of exposure indicates that NO initially adsorbs dissociatively at S_{vac} sites, followed by N_2 formation *via* recombinative desorption, leaving oxygen on the surface. Progressive exposure experiments further indicate that P2 (high-binding-energy O species) becomes more prominent at higher O coverage, suggesting O–O bond formation at S_{vac} sites.

DFT-D3 calculations indicate that NO dissociative adsorption is thermodynamically more favorable on the defective $FeS_2(100)$ surface than on the defect-free surface. Computed O 1s binding energies match experimental values, assigning P1 primarily to oxygen at S_{vac}, S atop, and (Fe–S)–O sites and assigning P2 to the lower oxygen atom in an O–O species at S_{vacs}. Two mechanistic pathways for N_2 formation and oxygen stabilization are proposed: (1) O–O at S_{vacs} and (2) interaction of oxygen with the neighboring surface sulfur dimer to form S_{mono}. Both are consistent with the observed oxygen and sulfur species under NO exposure.

Overall, the experimental and theoretical results presented in this study reveal a strong correlation between the S_{vac} concentration and NO dissociation reactivity on $FeS_2(100)$. SR-XPS measurements show that high S_{vac} densities markedly promote NO adsorption and facilitate dissociative reaction pathways. In addition, SR-XPS identified characteristic oxygen and nitrogen species remaining on the FeS_2 surfaces after NO exposure. DFT-D3 calculations clarified the possible surface oxygen species on $FeS_2(100)$ by directly computing absolute binding energies using the ΔSCF method. In addition, the energy diagram provided insight into the thermodynamic and mechanistic origins of the observed processes. These findings highlight the essential role of defect engineering in controlling surface reactivity and suggest that tuning S_{vac} populations on $FeS_2(100)$ surfaces offers a promising strategy for modulating catalytic behavior toward nitrogen oxides.

Author contributions

W. H.: experimental and theoretical investigation, visualization, writing – original draft and writing – review and editing; F. O.: experimental investigation, review and editing; K. M.: experimental investigation, review and editing; S. T.: experimental investigation, review and editing; D. H.: sample preparation from a natural crystal; M. F.: software and theoretical investigation; T. O.: calculational resources, software, and theoretical investigation; J. Y.: funding acquisition, supervision, investigation, writing – original draft and writing – review and editing.

Conflicts of interest

The authors declare no conflicts of interest.

Data availability

The data supporting this article have been included as part of the supplementary information (SI). Supplementary information is available. See DOI: https://doi.org/10.1039/d6cp00466k.

The data will be available from the corresponding author on reasonable request.

Acknowledgements

The present study was supported by the Transformative Research Areas (A) program "Geochemistry of CO worlds" (25H01695) of the Japan Society for the Promotion of Science (JSPS). This work was also supported by SPRING-GX of the University of Tokyo, Grant Number GXA240129. The computation in this work has been done using the facilities of the Supercomputer Center, the Institute for Solid State Physics, the University of Tokyo (2024-P-0014 and 2025-P-0001). Synchrotron radiation experiments were performed at the BL-13B of the Photon Factory under the approval of the PF-PAC (No. 2023G096 and 2025G133). We thank Prof. Kazuhiko Mase, Prof. Kenichi Ozawa, and the staff members of the Photon Factory for their technical support.

References

1 N. Gruber and J. N. Galloway, *Nature*, 2008, **451**, 293–296.
2 H. He, Y. Wang, Q. Ma, J. Ma, B. Chu, D. Ji, G. Tang, C. Liu, H. Zhang and J. Hao, *Sci. Rep.*, 2014, **4**, 4172.

3 I. Jhun, B. A. Coull, A. Zanobetti and P. Koutrakis, *Air Qual., Atmos. Health*, 2015, **8**, 283–292.
4 K. Li, D. J. Jacob, H. Liao, J. Zhu, V. Shah, L. Shen, K. H. Bates, Q. Zhang and S. Zhai, *Nat. Geosci.*, 2019, **12**, 906–910.
5 S. Rood, S. Eslava, A. Manigrasso and C. Bannister, *Proc. Inst. Mech. Eng., Part D*, 2020, **234**, 936–949.
6 M. V. Twigg, *Catal. Today*, 2011, **163**, 33–41.
7 J. Wang, H. Chen, Z. Hu, M. Yao and Y. Li, *Catal. Rev.*, 2015, **57**, 79–144.
8 J. Xia, J. Jiao, B. Dai, W. Qiu, S. He, W. Qiu, P. Shen and L. Chen, *RSC Adv.*, 2013, **3**, 6132–6140.
9 Z. Meng, F. Wei, W. Ma, N. Yu, P. Wei, Z. Wang, Y. Tang, Z. Chen, H. Wang and M. Zhu, *Adv. Funct. Mater.*, 2016, **26**, 8231–8242.
10 H. Choi, J. Y. Seo, Y. R. Uhm, G. M. Sun and C. S. Kim, *AIP Adv.*, 2021, 11.
11 M. Barawi, I. J. Ferrer, E. Flores, S. Yoda, J. R. Ares and C. Sánchez, *J. Phys. Chem. C*, 2016, **120**, 9547–9552.
12 H. Li, J. Liu, J. Li, Y. Hu, W. Wang, D. Yuan, Y. Wang, T. Yang, L. Li, H. Sun, S. Ren, X. Zhu, Q. Guo, X. Wen, Y. Li and B. Shen, *ACS Catal.*, 2017, **7**, 4805–4816.
13 Y. Tian, X. Zhou, M. Liu, J. Zhang, W. Wang, Z. Song and X. Zhao, *Chemosphere*, 2023, **340**, 139789.
14 H. Lee, R. Zheng, L. Huang, T. C. Germann, M. R. Gross and M. Mehana, *ACS Sustainable Chem. Eng.*, 2025, **13**, 4548–4559.
15 T. Liu, I. Temprano, S. J. Jenkins, D. A. King and S. M. Driver, *J. Phys. Chem. C*, 2013, **117**, 10990–10998.
16 T. Liu, I. Temprano, S. J. Jenkins, D. A. King and S. M. Driver, *Phys. Chem. Chem. Phys.*, 2012, **14**, 11491–11499.
17 M. Sacchi, M. C. Galbraith and S. J. Jenkins, *Phys. Chem. Chem. Phys.*, 2012, **14**, 3627–3633.
18 J. Y. Kim, Ł. Gelczuk, M. P. Polak, D. Hlushchenko, D. Morgan, R. Kudrawiec and I. Szlufarska, *npj 2D Mater. Appl.*, 2022, **6**, 75.
19 B. A. Hanedar and M. C. Onbaşlı, *Phys. Chem. Chem. Phys.*, 2025, **27**, 1809–1818.
20 A. T. Garcia-Esparza, S. Park, H. Abroshan, O. A. Paredes Mellone, J. Vinson, B. Abraham, T. R. Kim, D. Nordlund, A. Gallo and R. Alonso-Mori, *ACS Nano*, 2022, **16**, 6725–6733.
21 F. Ozaki, S. Tanaka, Y. Choi, W. Osada, K. Mukai, M. Kawamura, M. Fukuda, M. Horio, T. Koitaya, S. Yamamoto, I. Matsuda, T. Ozaki and J. Yoshinobu, *Chem. Phys. Chem.*, 2023, **24**, e202300477.
22 D. Escalera-López, C. Iffelsberger, M. Zlatar, K. Novčić, N. Maselj, C. Van Pham, P. Jovanovič, N. Hodnik, S. Thiele, M. Pumera and S. Cherevko, *Nat. Commun.*, 2024, **15**, 3601.
23 H. Li, C. Tsai, A. L. Koh, L. Cai, A. W. Contryman, A. H. Fragapane, J. Zhao, H. S. Han, H. C. Manoharan, F. Abild-Pedersen, J. K. Nørskov and X. Zheng, *Nat. Mater.*, 2016, **15**, 48–53.
24 Z. Meng, J. Fan, A. Chen and X. Xie, *Mater. Today Chem.*, 2023, **29**, 101449.
25 J. Hu, L. Yu, J. Deng, Y. Wang, K. Cheng, C. Ma, Q. Zhang, W. Wen, S. Yu, Y. Pan, J. Yang, H. Ma, F. Qi, Y. Wang, Y. Zheng, M. Chen, R. Huang, S. Zhang, Z. Zhao, J. Mao, X. Meng, Q. Ji, G. Hou, X. Han, X. Bao, Y. Wang and D. Deng, *Nat. Catal.*, 2021, **4**, 242–250.
26 M. G. Bianchi, F. Risplendi, M. Re Fiorentin and G. Cicero, *Adv. Sci.*, 2024, **11**, 2305162.
27 Q. Sun, M. Yuan, R. Wu, Y. Miao, Y. Yuan, Y. Jing, Y. Qu, X. Liu and J. Sun, *Adv. Mater.*, 2023, **35**, 2302318.
28 H. R. Inta, D. Dhanabal, S. S. Markandaraj and S. Shanmugam, *EES Catal.*, 2023, **1**, 645–664.
29 W. S. Epling, J. E. Parks, G. C. Campbell, A. Yezerets, N. W. Currier and L. E. Campbell, *Catal. Today*, 2004, **96**, 21–30.
30 F. Herbert, A. Krishnamoorthy, K. Van Vliet and B. Yildiz, *Surf. Sci.*, 2013, **618**, 53–61.
31 J. Lin, X. Lin, S. Lu, W. Liao, T. Qi, S. Liang, Z.-J. Zhao and L. Jiang, *Chem. Eng. Sci.*, 2024, **300**, 120664.
32 C. He, P. Shi, D. Pang, Z. Zhang and L. Lin, *Mol. Catal.*, 2022, **524**, 112327.
33 H. Li, X. Song, N. Zhang, K. Chu and J. Zhao, *J. Colloid Interface Sci.*, 2025, **678**, 242–250.
34 G. Wächtershäuser, *Prog. Biophys. Mol. Biol.*, 1992, **58**, 85–201.
35 T. Samuels, D. Pybus, M. Wilkinson and C. S. Cockell, *Geomicrobiol. J.*, 2019, **36**, 600–611.
36 L. Vincent, M. Berg, M. Krismer, S. T. Saghafi, J. Cosby, T. Sankari, K. Vetsigian, H. J. Cleaves and D. A. Baum, *Life*, 2019, **9**, 80.
37 T. Suzuki, T.-A. Yano, M. Hara and T. Ebisuzaki, *Surf. Sci.*, 2018, **674**, 6–12.
38 P. Lindgren, J. Parnell, N. G. Holm and C. Broman, *Geochem. Trans.*, 2011, **12**, 1–7.
39 S. Galvez-Martinez, E. Escamilla-Roa, M.-P. Zorzano and E. Mateo-Marti, *Phys. Chem. Chem. Phys.*, 2019, **21**, 24535–24542.
40 M. Sanchez-Arenillas and E. Mateo-Marti, *Phys. Chem. Chem. Phys.*, 2016, **18**, 27219–27225.
41 S. Galvez-Martinez, V. Pérez-Dieste, M. Sanchez-Arenillas, C. Escudero and E. Mateo-Martí, *Appl. Surf. Sci.*, 2025, **681**, 161536.
42 E. Mateo-Marti, S. Galvez-Martinez, C. Gil-Lozano and M.-P. Zorzano, *Sci. Rep.*, 2019, **9**, 15311.
43 K. J. Andersson, H. Ogasawara, D. Nordlund, G. E. Brown Jr and A. Nilsson, *J. Phys. Chem. C*, 2014, **118**, 21896–21903.
44 A. Toyoshima, T. Kikuchi, H. Tanaka, K. Mase, K. Amemiya and K. Ozawa, *J. Phys.: Conf. Ser.*, 2013, **425**, 152019.
45 T. Ozaki, *The code, OpenMX, pseudoatomic basis functions, and pseudopotentials*, can be found under https://www.openmx-square.org.
46 T. Ozaki and H. Kino, *Phys. Rev. B: Condens. Matter Mater. Phys.*, 2005, **72**, 045121.
47 J. P. Perdew, K. Burke and M. Ernzerhof, *Phys. Rev. Lett.*, 1996, **77**, 3865.
48 K. Lejaeghere, G. Bihlmayer, T. Björkman, P. Blaha, S. Blügel, V. Blum, D. Caliste, I. E. Castelli, S. J. Clark,

A. Dal Corso, S. de Gironcoli, T. Deutsch, J. K. Dewhurst, I. Di Marco, C. Draxl, M. Dułak, O. Eriksson, J. A. Flores-Livas, K. F. Garrity, L. Genovese, P. Giannozzi, M. Giantomassi, S. Goedecker, X. Gonze, O. Grånäs, E. K. U. Gross, A. Gulans, F. Gygi, D. R. Hamann, P. J. Hasnip, N. A. W. Holzwarth, D. Iuşan, D. B. Jochym, F. Jollet, D. Jones, G. Kresse, K. Koepernik, E. Küçükbenli, Y. O. Kvashnin, I. L. M. Locht, S. Lubeck, M. Marsman, N. Marzari, U. Nitzsche, L. Nordström, T. Ozaki, L. Paulatto, C. J. Pickard, W. Poelmans, M. I. J. Probert, K. Refson, M. Richter, G.-M. Rignanese, S. Saha, M. Scheffler, M. Schlipf, K. Schwarz, S. Sharma, F. Tavazza, P. Thunström, A. Tkatchenko, M. Torrent, D. Vanderbilt, M. J. van Setten, V. Van Speybroeck, J. M. Wills, J. R. Yates, G.-X. Zhang and S. Cottenier, *Science*, 2016, **351**, aad3000.

49 S. Grimme, S. Ehrlich and L. Goerigk, *J. Comput. Chem.*, 2011, **32**, 1456–1465.

50 S. Grimme, J. Antony, S. Ehrlich and H. Krieg, *J. Chem. Phys.*, 2010, 132.

51 T. Ozaki, *Phys. Rev. B: Condens. Matter Mater. Phys.*, 2003, **67**, 155108.

52 G. Theurich and N. A. Hill, *Phys. Rev. B: Condens. Matter Mater. Phys.*, 2001, **64**, 073106.

53 I. Morrison, D. M. Bylander and L. Kleinman, *Phys. Rev. B: Condens. Matter Mater. Phys.*, 1993, **47**, 6728–6731.

54 T. Ozaki, *Database of optimized VPS and PAO*, 2019, can be found under https://www.openmx-square.org/vps_pao2019/.

55 T. Ozaki and C.-C. Lee, *Phys. Rev. Lett.*, 2017, **118**, 026401.

56 M. Jarvis, I. White, R. Godby and M. C. Payne, *Phys. Rev. B: Condens. Matter Mater. Phys.*, 1997, **56**, 14972.

57 F. Ozaki, S. Tanaka, Y. Choi, W. Osada, K. Mukai, M. Kawamura, M. Fukuda, M. Horio, T. Koitaya and S. Yamamoto, *Chem. Phys. Chem.*, 2023, **24**, e202300477.

58 W. Osada, M. Hasegawa, Y. Shiozawa, K. Mukai, S. Yoshimoto, S. Tanaka, M. Kawamura, T. Ozaki and J. Yoshinobu, *Phys. Chem. Chem. Phys.*, 2025, **27**, 1978–1989.

59 C.-C. Lee, J. Yoshinobu, K. Mukai, S. Yoshimoto, H. Ueda, R. Friedlein, A. Fleurence, Y. Yamada-Takamura and T. Ozaki, *Phys. Rev. B*, 2017, **95**, 115437.

60 C.-C. Lee, B. Feng, M. D'Angelo, R. Yukawa, R.-Y. Liu, T. Kondo, H. Kumigashira, I. Matsuda and T. Ozaki, *Phys. Rev. B*, 2018, **97**, 075430.

61 A. Fleurence, C. C. Lee, R. Friedlein, Y. Fukaya, S. Yoshimoto, K. Mukai, H. Yamane, N. Kosugi, J. Yoshinobu, T. Ozaki and Y. Yamada-Takamura, *Phys. Rev. B*, 2020, **102**, 201102.

62 L. Patterer, P. Ondračka, D. Bogdanovski, L. Jende, S. Prünte, S. Mráz, S. Karimi Aghda, B. Stelzer, M. Momma and J. M. Schneider, *Appl. Surf. Sci.*, 2022, **593**, 153363.

63 K. Momma and F. Izumi, *Appl. Crystallogr.*, 2011, **44**, 1272–1276.

64 K. Momma and F. Izumi, *Appl. Crystallogr.*, 2008, **41**, 653–658.

65 T. Marshall-Roth, N. J. Libretto, A. T. Wrobel, K. J. Anderton, M. L. Pegis, N. D. Ricke, T. V. Voorhis, J. T. Miller and Y. Surendranath, *Nat. Commun.*, 2020, **11**, 5283.

66 J. M. Guevremont, D. R. Strongin and M. A. Schoonen, *Am. Mineral.*, 1998, **83**, 1246–1255.

67 A. P. Chandra and A. R. Gerson, *Geochim. Cosmochim. Acta*, 2011, **75**, 6239–6254.

68 S. Abujarada, A. S. Walton, A. G. Thomas, U. K. Chohan and S. P. Koehler, *Phys. Chem. Chem. Phys.*, 2019, **21**, 10939–10946.

69 A. Pashutski and M. Folman, *Surf. Sci.*, 1989, **216**, 395–408.

70 A. G. Schaufuß, H. W. Nesbitt, I. Kartio, K. Laajalehto, G. M. Bancroft and R. Szargan, *J. Electron Spectrosc. Relat. Phenom.*, 1998, **96**, 69–82.

71 A. Buckley and R. Woods, *Appl. Surf. Sci.*, 1987, **27**, 437–452.

72 H. Nesbitt and I. Muir, *Geochim. Cosmochim. Acta*, 1994, **58**, 4667–4679.

73 H. Nesbitt, M. Scaini, H. Hochst, G. Bancroft, A. Schaufuss and R. Szargan, *Am. Mineral.*, 2000, **85**, 850–857.

74 J. Leiro, S. Mattila and K. Laajalehto, *Surf. Sci.*, 2003, **547**, 157–161.

75 K. Andersson, M. Nyberg, H. Ogasawara, D. Nordlund, T. Kendelewicz, C. Doyle, G. Brown Jr, L. Pettersson and A. Nilsson, *Phys. Rev. B: Condens. Matter Mater. Phys.*, 2004, **70**, 195404.

76 F. Herbert, A. Krishnamoorthy, W. Ma, K. Van Vliet and B. Yildiz, *Electrochim. Acta*, 2014, **127**, 416–426.

